Journal of Materials Chemistry A

Cite this: J. Mater. Chem. A, 2019, 7, 17966

V_2O_5–Conductive polymer nanocables with built-in local electric field derived from interfacial oxygen vacancies for high energy density supercapacitors†

Wenchao Bi,[ab] Juanjuan Huang,[bc] Mingshan Wang,[bd] Evan P. Jahrman,[e] Gerald T. Seidler,[e] Jichao Wang,[a] Yingjie Wu,[f] Guohua Gao,[*ag] Guangming Wu*[a] and Guozhong Cao[*b]

Received 24th April 2019
Accepted 27th June 2019

DOI: 10.1039/c9ta04264d

rsc.li/materials-a

Generating oxygen vacancies (Vö) in vanadium pentoxide (V_2O_5) has been demonstrated as an effective approach to tailor its electrochemical properties. The present study investigates three different kinds of conductive polymer (CP = PPy, PEDOT, and PANI) coated V_2O_5 nanofibers with Vö generated at the interface during the polymerization process. Surface Vö form a local electric field and promote the charge transfer kinetics of the resulting Vö-V_2O_5/CP nanocables, and the accompanying V^{4+} and V^{3+} ions may also catalyze the redox reactions and improve the supercapacitor performance. The differences and similarities of three different CP coatings have been compared and discussed, and are dependent on their polymerization conditions and coating thickness. The distribution of Vö in the surface layer and in the bulk has been elaborated and the corresponding effects on the electrochemical properties and supercapacitor performance have also been investigated. Vö-V_2O_5/CP can deliver a high capacity of up to 614 F g^{-1} at a current rate of 0.5 A g^{-1} and supercapacitors with Vö-V_2O_5/CP demonstrated excellent cycling stability over 15 000 cycles at a rate of 10 A g^{-1}.

Introduction

Supercapacitors (SCs) are appealing energy storage devices that have gained overwhelming attention due to their high power density, long cycling duration, safety, sustainability, and low-cost.[1–5] Rechargeable aqueous SCs will play a critical role in large-scale deployment of intermittent renewable energy sources, smart power grids, and electric vehicles.[6–8] Due to the above advantages, substantial efforts have been directed toward the development of SCs with a higher energy density to meet the ever-increasing requirements. In particular, much research has targeted electrode materials which greatly affect the electrochemical performance of SCs.[9–11] Transition metal oxides (TMOs) have promising applications in electrochemical energy storage due to their high theoretical specific capacitance and high energy density.[12,13]

Vanadium pentoxide (V_2O_5), one such TMO, is appealing in electrochemical energy storage due to its high theoretical capacitance (2020 F g^{-1}), large voltage window (up to ~2.8 V), low cost, and abundance.[14,15] Despite these advantages, the commercial viability of V_2O_5-based SCs is diminished by the low electrical conductivity of V_2O_5 (10^{-3} to 10^{-2} S cm^{-1}) and cycling instability, leading to unsatisfactory practical performance. Defects, especially oxygen vacancies (Vö), could effectively improve the electrochemical performance of TMOs by adjusting their electronic structure while leaving the lattice as a whole largely unchanged.[16] Specifically, Vö can promote charge transfer kinetics with a larger interlayer spacing and allow the structure to be retained during cycling, and have thus been proposed to improve the specific capacitance and prolong the cycling duration of TMOs.[17–19] Conductive polymers (CPs), such as poly(3,4-ethylenedioxythiophene) (PEDOT),[20] polypyrrole (PPy),[21] and polyaniline (PANI), could also improve the electrical conductivity of V_2O_5.[22] Gradient Vö on the V_2O_5 nanofiber (V_2O_5-NF) surface induced by PEDOT polymerization demonstrated

[a]Shanghai Key Laboratory of Special Artificial Microstructure Materials and Technology, School of Physics Science and Engineering, Tongji University, Shanghai 200092, China. E-mail: gao@tongji.edu.cn; wugm@tongji.edu.cn

[b]Department of Materials Science and Engineering, University of Washington, Seattle, WA 98195-2120, USA. E-mail: gzcao@u.washington.edu

[c]MOE Key Laboratory for Magnetism and Magnetic Materials, School of Physical Science and Technology, Lanzhou University, Lanzhou 730000, China

[d]School of Materials Science and Engineering, Southwest Petroleum University, Chengdu, Sichuan 610500, PR China

[e]Department of Physics, University of Washington, Seattle, WA 98195-1560, USA

[f]Department of Material Science and Engineering, Monash University, Clayton, Victoria 3800, Australia

[g]Key Laboratory of Road and Traffic Engineering of the Ministry of Education, Tongji University, Shanghai 201804, China

† Electronic supplementary information (ESI) available: Digital images, TG-DSC curves, XPS, HRTEM, CV and GCD curves. See DOI: 10.1039/c9ta04264d

much improved electrochemical properties and resulted in supercapacitor performance with facilitated charge transfer kinetics, and promoted redox reactions.[23] It was further revealed that the concentration of Vö on the V_2O_5-NF surface, through tailoring the polymerization of PEDOT, has an appreciable influence on the electrochemical properties and device performance.[24] Since all PPy, PANI and PEDOT are CPs and have been widely applied in supercapacitors, it is interesting to explore if all these three different kinds of CPs would generate Vö on the surface of V_2O_5-NFs through a similar oxidative polymerization process, and how different CP coatings would work synergistically with Vö to influence the electrochemical properties and performance of V_2O_5-NFs.

In this work, Vö are induced at the interface of V_2O_5-NFs with different kinds of CPs (CP = PEDOT, PPy and PANI) to improve the electrochemical performance of the obtained Vö-V_2O_5/CP nanocables for high-performance supercapacitors. In a similar oxidative polymerization process, different thicknesses of CP coatings are obtained, and the induced Vö promote the charge transfer kinetics of the resulting Vö-V_2O_5/CP nanocables by forming a local electric field, and the accompanying V^{4+} and V^{3+} may also catalyze the redox reactions and improve the supercapacitor performance. The detailed relationships between the properties of CPs, the thickness of CP coatings, the overall concentration of Vö, charge transfer kinetics, the electrochemical properties and the supercapacitor performance are investigated and discussed.

Experimental section

Materials characterization

XRD patterns of the as-prepared samples were obtained using an X-ray diffractometer (XRD, Bruker D8 Advance, Germany) with a Rigaku D/max-C diffractometer and Cu-Kα (λ = 0.15406 nm) radiation. FTIR was performed using a Bruker-TENSOR27 FTIR spectrometer from 400 to 4000 cm^{-1}. TG-DSC analysis was performed using a SDT Q600 at a temperature from 25 to 800 °C, and a heating rate of 10 °C min^{-1} in flowing air. Field emission scanning electron microscopy (FESEM, S-4800, Japan) and transmission electron microscopy (TEM, JEOLR2100, Japan) were employed to characterize the morphologies of all samples. XPS with Mg Kα radiation ($h\nu$ = 1253.6 eV) performed using a PHI-5000C ESCA system was used to examine the surface vanadium oxidation states of all samples. X-ray absorption near edge structure (XANES) measurements (University of Washington) were performed at the vanadium K-edge with laboratory-based instrumentation to assess the bulk vanadium oxidation state distribution of all samples.[25,26] The analysis and fitting were performed using a previously reported methodology.[23]

Electrochemical measurements

The electrodes were prepared by painting a slurry (active materials, acetylene black and poly(vinylidene fluoride) (PVDF) in *N*-methylpyrrolidone (NMP) with a mass ratio of 8 : 1 : 1) onto a graphite paper current collector, and then drying under vacuum at 120 °C overnight. The electrodes were tested in a symmetric-electrode test cell and 1 M Na_2SO_4 solution. Cyclic voltammetry (CV), galvanostatic charge/discharge (GCD) and electrochemical impedance spectroscopy (EIS) were performed on a CHI660C (Chenhua) electrochemical working station (−1 to 1 V)[23] with scan rates from 5 to 10, 25, 50 and 100 mV s^{-1} for CV, and current densities GCD from 0.5 to 1, 2.5, 5 and 10 A g^{-1}. EIS was performed in the frequency from 10 mHz to 100 kHz with an AC voltage amplitude of 5 mV. The specific capacitance of each electrode (C, F g^{-1}) was obtained from the GCD curves of the discharging process using the equation $C = 2I\Delta t/(m\Delta V)$, where I is the constant discharge current, m is the total mass of each electrode, Δt is discharging duration and ΔV is the voltage window. The energy density (E, W h kg^{-1}) and power density (P, W kg^{-1}) in Ragone plots were calculated using the equations $E = (1/8)C(\Delta V)^2/3600$ and $P = E/\Delta t$, respectively.[24]

Preparation of Vö-V_2O_5/CP nanocables

The synthesis of Vö-V_2O_5/CP is schematically illustrated in Fig. 1. V_2O_5-NFs are fabricated according to a reported method.[27] V_2O_5-NFs are treated with hydrochloric acid vapours (HCl, 0.5 ml 36 wt%) in a vacuum at room temperature for 1 h, as shown in step 1. In step 2, the V_2O_5-NFs are moved to another vacuum container followed by the addition of 0.5 ml CP monomers (aniline, EDOT or pyrrole). Considering the different boiling points (found in product Safety Data Sheet, Sigma-Aldrich, 760 mm Hg) of pyrrole (129 °C), aniline (184.1 °C) and EDOT (193 °C), the polymerization temperature used for aniline and EDOT is 80 °C for 6 h, while pyrrole is polymerized at room temperature for uniform polymerization. Then the monomers polymerize on the surface of V_2O_5-NFs, forming a nanocable structure with Vö induced at the interface. The sample color changes from yellow to dark green (Fig. S1†). Then, Vö-V_2O_5/CP nanocables are dried in a vacuum oven at 120 °C overnight.

Results and discussion

In the synthesis process, Vö are induced at the interface of Vö-V_2O_5/CP nanocables. The polymerization process of CPs includes electron (e') loss and deprotonation (H^+).[28] As oxygen

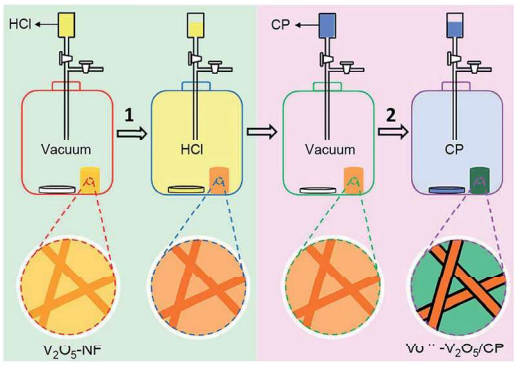

Fig. 1 Schematic diagram for the synthesis of Vö-V_2O_5/CP (CP = PANI, PEDOT or PPy) nanocables.

($O_o^{\times}$) in the V_2O_5 primitive lattice can donate electrons and generate Vö and O″, H_2O will form from O″ and H^+, and $V_v^{\times}$ in V_2O_5 receive electrons. Therefore, taking PPy for example, the possible reactions (1–4) are as follows.

$$nC_4H_5N - (2n-2)e' \rightarrow H(C_4H_2NH)_nH + (2n-2)H^+ \quad (1)$$

$$O_o^{\times} = Vö + O'' \quad (2)$$

$$2H^+ + O'' \rightarrow H_2O(g) \quad (3)$$

$$V_v^{\times} + e' \rightarrow V_v', \; V_v' + e' \rightarrow V_v'' \quad (4)$$

Thus, the above reactions can be presented as follows.

$$nC_4H_5N + (2n-2)V_v^{\times} + (n-1)O_o^{\times} \rightarrow H(C_4H_2NH)_nH + (n-1)H_2O(g) + mV_v^{\times'} + \left(n-1-\frac{1}{2}m\right)V_v^{\times''} + (n-1)Vö \quad (5)$$

Based on the above analysis, the concentration of Vö is directly related to the polymerization process.

Fourier transform infrared (FT-IR) spectra (Fig. 2a) of all samples exhibit the characteristic bands of V_2O_5-NFs with the stretching absorption modes of V=O bonds (1022 cm^{-1}) and V–O–V bonds (853, 520, and 483 cm^{-1}).[29] As for Vö-V_2O_5/PPy, the presence of PPy is shown (marked with #) by C=C or C–C bonds in the pyrrole ring (1545 and 1460 cm^{-1}), in-plane deformations of C–H, C–N and N–H bonds (1319, 1045, 1175, and 1093 cm^{-1}) and out-of plane deformations of C–H bonds (968 cm^{-1}).[30] For Vö-V_2O_5/PEDOT, the presence of PEDOT (marked with +) is shown by aromatic C=C and C–C bonds (1522 and 1397 cm^{-1}), C–O–C bonds (1207, 1143, and 1090 cm^{-1}), and C–S bonds (934, 833, and 692 cm^{-1}).[31] The main characteristic bands of PANI (marked with *) in Vö-V_2O_5/PANI are attributed to aromatic C=C and C=N bonds (1634, 1587, and 1502 cm^{-1}), C–N, C–H bonds (1300 and 1172 cm^{-1}), and the aromatic ring and out-of-plane deformation (692 and 633 cm^{-1}).[32,33]

Thermogravimetry (TG) and differential scanning calorimetry (DSC) measurements in Fig. S2† show that the mass ratios of PPy, PEDOT and PANI in the corresponding composites are ~18%, ~27% and ~40%, respectively.[30] Compared with PEDOT, the larger percentage of PANI should be attributed to the lower boiling point and the smaller molecular weight (obtained from product Safety Data Sheet, Sigma-Aldrich) of the aniline monomer (184.1 °C, 93.1 g mol^{-1}) than the EDOT monomer (193 °C, 142.2 g mol^{-1}). Although pyrrole possesses a lower boiling point and smaller molecular weight (129 °C, 67.1 g mol^{-1}) than aniline and EDOT, the higher reaction temperature of PANI (80 °C) and PEDOT (80 °C) than PPy (room temperature) would accelerate the polymerization.[34]

In Fig. 2b, the X-ray diffraction (XRD) patterns display a pure V_2O_5 phase (JCPDS no. 85-0601) in all samples, suggesting an

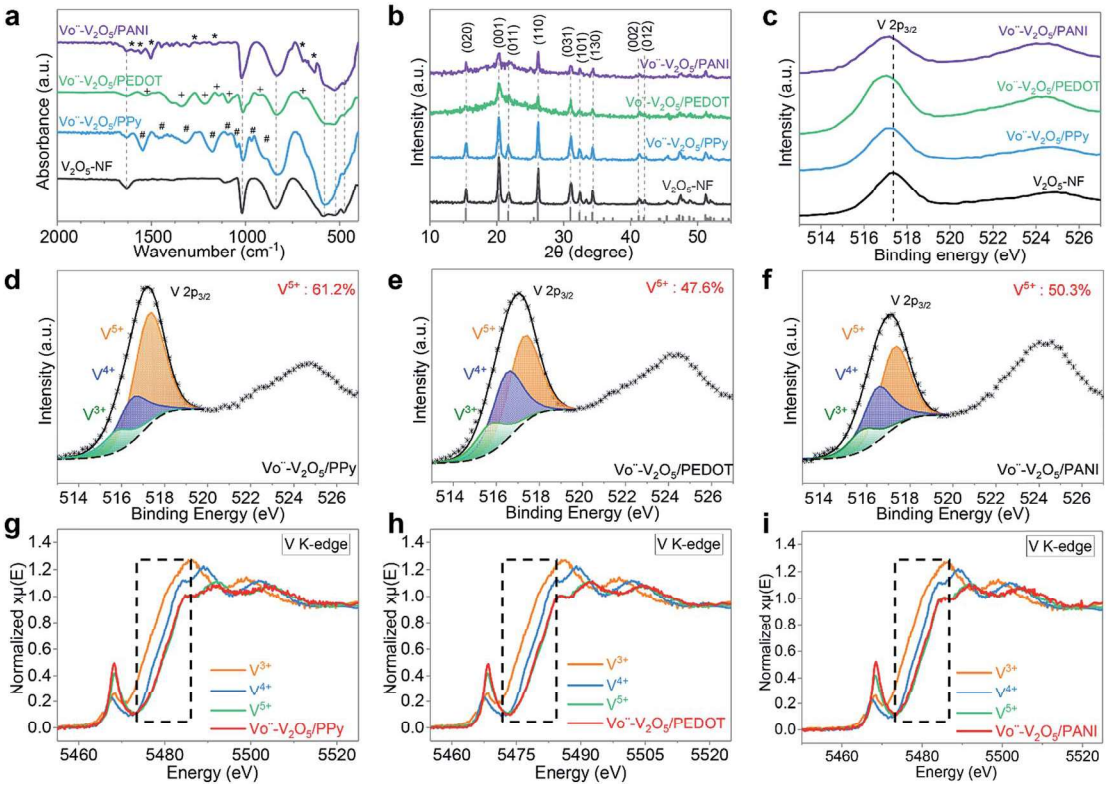

Fig. 2 (a) FTIR spectrum, (b) XRD patterns of Vö-V_2O_5/CPs and V_2O_5-NFs. (c) V 2p peaks in the XPS spectrum of Vö-V_2O_5/CPs and V_2O_5-NFs. (d–f) The decomposition of the V $2p_{3/2}$ peak of Vö-V_2O_5/CPs. (g–i) The V K-edge XANES spectra of Vö-V_2O_5/CPs alongside empirical standards. The dashed box denotes the general vicinity of the V K-edge for these materials.

unchanged crystalline structure during the polymerization process. The broadened and lower intensity peaks in Vö-V_2O_5/CPs indicate the evolution of an amorphous phase, which might be caused by Vö and CPs.

X-ray photoelectron spectroscopy (XPS) investigated the oxidation states of vanadium on the surface of Vö-V_2O_5/CPs. As shown in Fig. 2c, relative to V_2O_5-NFs, the V $2p_{3/2}$ peaks of all Vö-V_2O_5/CPs move toward lower binding energies, indicating the reduction of Vö-V_2O_5/CPs. Considering that the XRD patterns show a pure V_2O_5 phase, the reduction should be caused by Vö. The detailed decomposition of the V $2p_{3/2}$ peak shows three peaks for V^{5+}, V^{4+} and V^{3+} as shown in Fig. 2d–f and S3.† The calculated concentration of V^{5+} in Vö-V_2O_5/PPy, Vö-V_2O_5/PANI and V_2O_5-NFs is 61.2%, 47.6%, 50.5% and 91.2%, respectively, and the corresponding concentration of Vö (0.5V^{4+} and V^{3+}) is 26.0%, 34.2%, and 31.9%. Thus, Vö are induced in Vö-V_2O_5/CPs by the polymerization of PPy, PEDOT and PANI. Further examination of the oxidation state of vanadium atoms in the system was carried out with X-ray absorption near edge structure (XANES) measurements. These measurements provided insight into Vö concentrations in the bulk of each sample and complemented the XPS results which only characterized the shallow surface of each sample and might be less representative of the speciation in the bulk, especially with thick CP coatings on the surface of V_2O_5-NFs. The V K-edge XANES spectra of Vö-V_2O_5/CPs are shown with respect to those of commercial V_2O_3, VO_2 and V_2O_5, which served as empirical standards.[23] The early stages of an edge shift are observed in the XANES spectra of Vö-V_2O_5/PPy (Fig. 2g), Vö-V_2O_5/PEDOT (Fig. 2h) and Vö-V_2O_5/PANI (Fig. 2i), respectively. As an edge shift to lower photon energies corresponds to the reduction of the probed element, this suggests that Vö are present in Vö-V_2O_5/CPs, which is consistent with XPS and XRD analyses. However, the general agreement between Vö-V_2O_5/CPs and the V_2O_5 spectra reveals that the bulk of the V atoms remains as V^{5+}. Indeed, fitting results show a smaller percentage of Vö (0.2% for Vö-V_2O_5/PPy, 1.3% for Vö-V_2O_5/PEDOT and 5.4% for Vö-V_2O_5/PANI, respectively) than the XPS results, confirming the near-surface modification of Vö. Moreover, the overall concentration of Vö is generally consistent with the corresponding CP content from the above TG results.

Scanning electron microscopy (SEM) and transmission electron microscopy (TEM) images of Vö-V_2O_5/CPs show that V_2O_5-NFs are coated homogeneously with a ~6.7 nm PANI layer (Fig. 3a, d and g), a ~5.0 nm PEDOT layer (Fig. 3b, e and h), and a ~3.5 nm PPy layer (Fig. 3c, f and i), respectively. These thicknesses of the CP shell are roughly consistent with the above mass ratios. The even distributions of CP coatings are visually confirmed from high-angle annular dark-field scanning transmission electron microscopy (HAADF-STEM) images and the corresponding elemental mappings, where the characteristic elements of CPs are distributed uniformly, as shown in Fig. 3m–o. In Fig. 3j, further characterization of a high-resolution TEM (HRTEM) image by inverse fast Fourier transform (IFFT) demonstrates dislocations with blurred lattice fringes in Vö-V_2O_5/PANI with an expanded interplanar spacing ranging from 5.93 to 6.29 Å (standard parameter is 5.76 Å), corresponding to the (020) crystal planes of V_2O_5. Moreover, the distorted lattice fringes are easily visible and arise from Vö which cause the skewing of vanadium atoms around the Vö in V_2O_5. Similarly, the interplanar spacing of the (011) crystal planes of V_2O_5 in Vö-V_2O_5/PEDOT increases from 4.09 Å (standard parameter) to 4.25 Å as shown in Fig. 3k, and that of the (020) planes in Vö-V_2O_5/PPy is between 5.76 and 5.84 Å as shown in **Fig. 3l**. Detailed information is provided in Fig. S4.† These

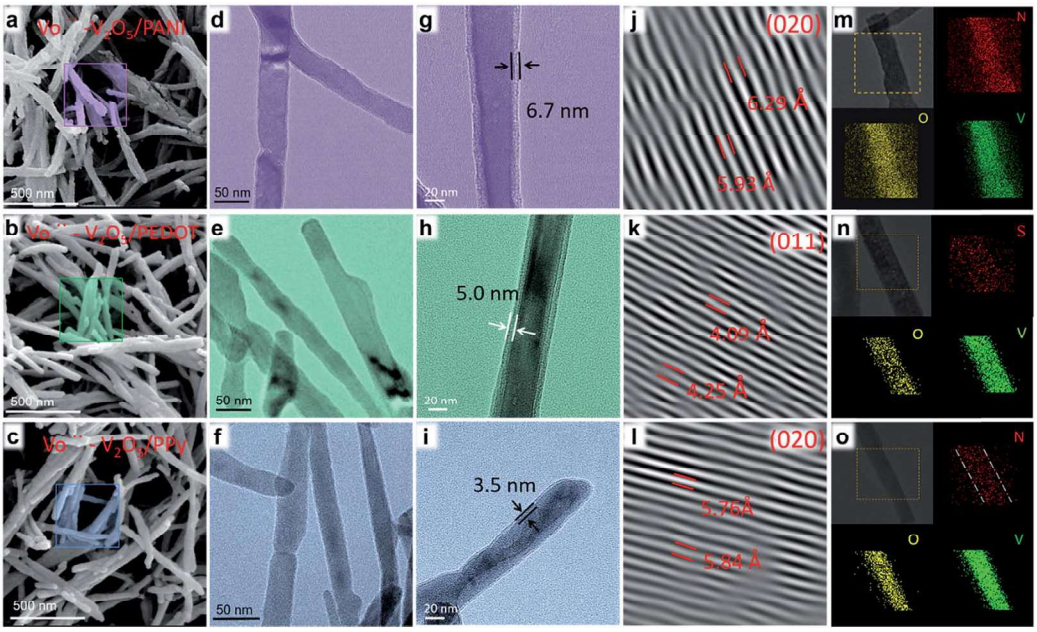

Fig. 3 (a–c) SEM images, (d–i) TEM images, (j–l) IFFT images, (m–o) HAADF-STEM images and the corresponding element mappings of Vö-V_2O_5/CPs.

IFFT images directly evidence the existence of Vö in Vö-V_2O_5/CPs. Based on all the above structural and morphological analyses, it is clear that Vö are generated in Vö-V_2O_5/CPs by PANI, PEDOT and PPy coatings.

The electrochemical potential of Vö-V_2O_5/CPs is evaluated using symmetrical double-supercapacitors (1 M Na_2SO_4 aqueous solution). The supercapacitive storage behavior is initially investigated by using cyclic voltammetry (CV). In Fig. 4a and S5,† the CV curves of all samples appear with nearly rectangular shapes. This reveals excellent reversible redox capacities although without redox peaks, which is widely accepted as a result of the fast, reversible successive multiple surface redox reactions.[35] Compared with other samples, Vö-V_2O_5/PEDOT possesses a larger voltammogram area, indicating higher supercapacitive performance (Fig. 4a). Consistently, the GCD curves of Vö-V_2O_5/CPs are nearly linear and symmetrical at various current densities (Fig. S6†). The specific capacitances of Vö-V_2O_5/PEDOT (614 F g^{-1}), Vö-V_2O_5/PANI (523 F g^{-1}) and Vö-V_2O_5/PPy (437 F g^{-1}) are obviously superior to that of V_2O_5-NFs (225 F g^{-1}) at 0.5 A g^{-1} (Fig. 4b). Vö-V_2O_5/CPs show larger specific capacitances than V_2O_5-NFs even at a high current density of 10 A g^{-1}, as shown in Fig. 4c. When the power density is 2500 W kg^{-1}, the energy densities of Vö-V_2O_5/PEDOT, Vö-V_2O_5/PPy and V_2O_5-NFs are 85, 73, 61 and 31 W h kg^{-1}, respectively (Fig. 4d). The enhancement in the capacitance may be attributed to interface modifications of Vö and CP shells, which will be further explored in the following text.

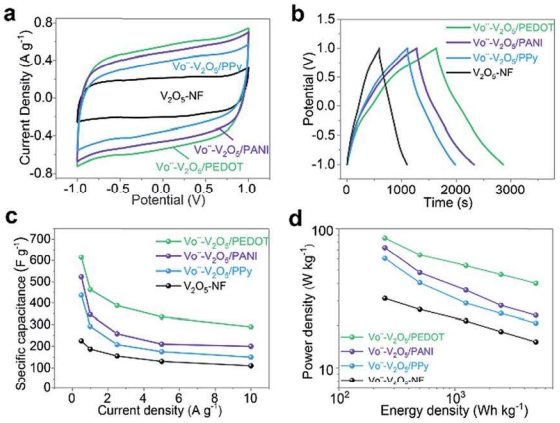

Fig. 4 (a) CV curves of Vö-V_2O_5/CPs and V_2O_5-NFs at a scan rate of 5 mV s^{-1}. (b) GCD curves of Vö-V_2O_5/CPs and V_2O_5-NFs at a current density of 0.5 A g^{-1}. (c) Specific capacitances of Vö-V_2O_5/CPs and V_2O_5-NFs at different current densities. (d) Ragone plots of Vö-V_2O_5/CPs and V_2O_5-NFs.

The role of Vö in promoting charge transfer kinetics during the charging and discharging processes was first analyzed. Fig. 5a shows the crystal structure of V_2O_5 and images viewed along the [010] and [001] directions. There are three kinds of vacancy sites in V_2O_5 according to the type of oxygen, including vanadyl oxygen (site 1), bridge oxygen (site 2) and chain oxygen (site 3), as shown in Fig. 5b. As vanadyl oxygen (site 1) has been reported as the easiest site to generate Vö,[36] the subsequent analyses will focus on Vö located at site 1. With skewing of vanadium atoms around the Vö sites, which was observed as dislocations in the above IFFT images, the charge distribution around Vö sites is off balance in the V_2O_5 plane, forming a positive region in the Vö center and a corresponding negatively charged area around Vö. During the discharging process, as illustrated in Fig. 5c, due to the imbalanced charge distribution, an extra electric field is formed in the direction from the non-Vö area to the negatively charged region, and Na^+ ions in the electrolyte will be attracted by coulombic forces and move to the negatively charged region around Vö. When it is fully discharged, the negatively charged area will be electrically neutral. During the charging process, a local electric field is formed in the direction from the positive Vö center to the neutral Na^+ accumulation region, and the corresponding coulombic forces will accelerate the migration of Na^+ ions away from the Vö center. Thus, the ionic transfer dynamics in V_2O_5-NFs is

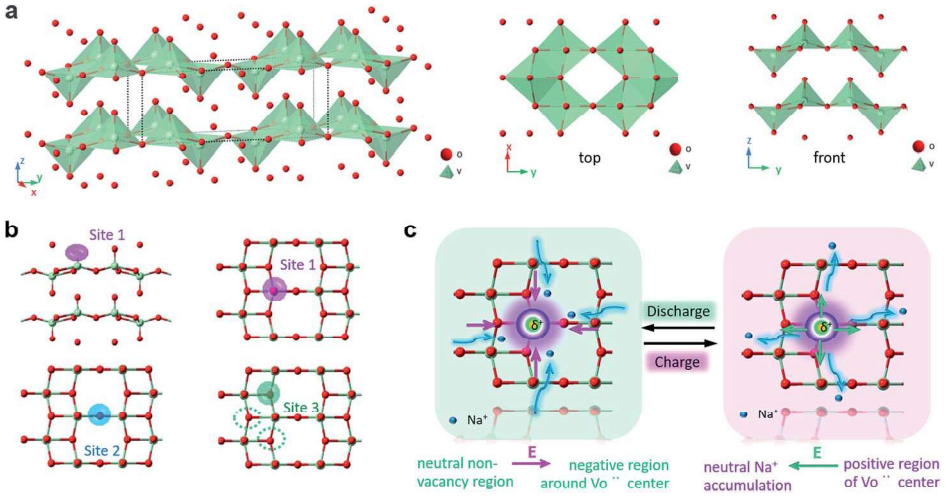

Fig. 5 (a) The crystal structure of V_2O_5 along the [010] and [001] directions. (b) The three kinds of sites for Vö in the V_2O_5 bulk structure. (c) Schematic illustration of the enhanced ionic transfer kinetics around Vö by the formation of a local electric field (E).

enhanced due to the local electric field caused by Vö, which was reported in Li-ion batteries as well.[37]

The kinetic reasons behind the high specific capacitances were further studied by electrochemical impedance spectroscopy (EIS). As shown in Fig. 6a, the interfacial charge transfer resistance (R_{ct}) of Vö-V_2O_5/PPy (5.9 Ω), Vö-V_2O_5/PEDOT (2.3 Ω) and Vö-V_2O_5/PANI (3.0 Ω) is smaller than that of V_2O_5-NFs (8.4 Ω), which suggests enhanced electronic transfer. The ion diffusion coefficients were calculated according to the formula:[38]

$$D - \frac{R^2T^2}{2A^2n^4F^4C^2\sigma_w{}^2} \quad (6)$$

The calculated Na^+ ion diffusion coefficients for all three Vö-V_2O_5/CPs are summarized in Table S1.† All Vö-V_2O_5/PPy (4.12×10^{-12}), Vö-V_2O_5/PEDOT (9.54×10^{-12} cm^2 s^{-1}) and Vö-V_2O_5/PANI (5.17×10^{-12}) show higher diffusion coefficient values than V_2O_5-NFs (2.51×10^{-12} cm^2 s^{-1}). The excellent specific capacitance of Vö-V_2O_5/CPs is likely attributed to improved charge transfer kinetics due to the synergistic combination of CP coatings and Vö. Vö provide void sites to accept/donate electrons and induce a local electric field to enhance the Na^+ ion transfer dynamics (discussed above). The accompanied V^{4+} and V^{3+} would also exert catalytic effects to promote the redox reactions and lead to enhanced capacitance.[39] Moreover, the CP coatings provide short and highly conductive pathways for rapid charge transfer, synergistically facilitating charge storage and improving the specific capacitance. The synergistic effects of the CP coating and Vö were further proven, taking Vö-V_2O_5/PANI for example, by physically mixing V_2O_5-NFs and commercial PANI. The obtained m-V_2O_5/PANI composite (without Vö) delivers a higher capacitance (312 F g^{-1}) than V_2O_5-NFs (225 F g^{-1}), but much lower than that of Vö-V_2O_5/PANI (523 F g^{-1}) at 0.5 A g^{-1} (the details can be found in Fig. S7, ESI†).

Fig. 6b shows that the Vö-V_2O_5/PEDOT electrode possesses a larger D_{Na^+} value and a smaller R_{ct} value (9.54×10^{-12} cm^2 s^{-1}, 2.3 Ω) than Vö-V_2O_5/PANI (5.17×10^{-12} cm^2 s^{-1}, 3.0 Ω) and Vö-V_2O_5/PPy (4.12×10^{-12} cm^2 s^{-1}, 5.9 Ω), and the specific capacitance of Vö-V_2O_5/PEDOT (614 F g^{-1}) is higher than that of Vö-V_2O_5/PANI (523 F g^{-1}) and Vö-V_2O_5/PPy (437 F g^{-1}). This suggests that Vö-V_2O_5/PEDOT is most favorable for electrolyte ion diffusion at the electrode–solution interface and electronic transfer, and thus leads to the most efficient charge storage among Vö-V_2O_5/CPs. Interestingly, the overall concentration of Vö in Vö-V_2O_5/PEDOT (1.3%) is larger than that in Vö-V_2O_5/PPy (0.3%), but smaller than that in Vö-V_2O_5/PANI (5.2%). This can be explained by the fact that, besides Vö, the CP coating synergistically improves the charge transfer kinetics of Vö-V_2O_5/CPs. Theoretically, the electrical resistance (R) is related to the electrical conductivity (σ), cross sectional area (A) and length (L), according to the electrical resistance formula $R = L/\sigma A$. From the different thicknesses of PPy (3.5 nm), PEDOT (5.0 nm) and PANI (6.7 nm), and the reported σ values of PEDOT (300–500 S cm^{-1}), PANI (0.1–5 S cm^{-1}) and PPy (10–50 S cm^{-1}),[40] the R value was estimated (Table S2, ESI†), and it shows that the calculated R of Vö-V_2O_5/PEDOT (17–28 Ω nm^{-1}) is smaller than that of Vö-V_2O_5/PANI (1239–61 941 Ω nm^{-1}) and Vö-V_2O_5/PPy (247–1237 Ω nm^{-1}). Thus, the combination of high electrical conductivity of PEDOT and Vö leads to the high specific capacitance of Vö-V_2O_5/PEDOT. This means that both the CP type and Vö concentration should be considered to improve the electrochemical performance of V_2O_5 (Table 1).

The cycling performance was tested at 10 A g^{-1}, as shown in Fig. 6c. After 15 000 cycles, Vö-V_2O_5/PEDOT, and Vö-V_2O_5/PPy show 111%, 108% and 101% capacitance retention, respectively. The excellent cyclability can be attributed to positively charged Vö which balance the strain and stress from adjacent layers and inhibit the structural collapse of V_2O_5,[16] as well as to the CP shells which protect the V_2O_5 core during the cycling process.[30] As the electric field drives surface-distributed Vö to

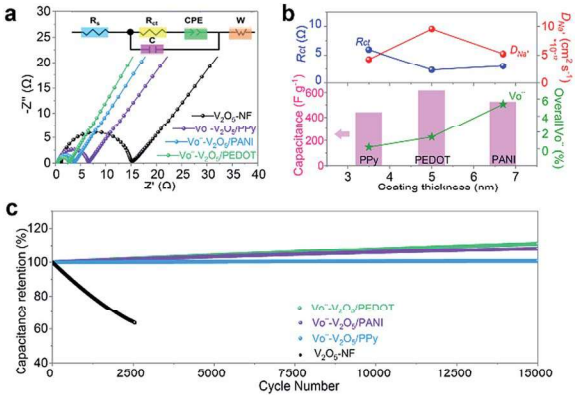

Fig. 6 (a) Nyquist plots of Vö-V_2O_5/CPs and V_2O_5-NFs. (b) Relationships between the coating thickness, R_{ct}, D_{Na^+}, overall Vö concentrations and specific capacitances of Vö-V_2O_5/CPs. (c) Cycling performance of Vö-V_2O_5/CPs and V_2O_5-NFs at 10 A g^{-1}.

Table 1 The related data of Vö-V_2O_5/CPs, including reaction temperature, physical and electrochemical properties, and the resulting supercapacitor performance

	Vö-V_2O_5/PPy	Vö-V_2O_5/PEDOT	Vö-V_2O_5/PANI
Monomer's molecular weight (g mol^{-1})	67.1	142.2	93.1
Monomer's boiling point (°C)	129	193	184
Reaction temperature (°C)	25	80	80
Mass content	18%	27%	40%
Coating thickness (nm)	3.5	5.0	6.5
Surface Vö (XPS)	26.0%	34.2%	31.9%
Overall Vö (XANES)	0.2%	1.3%	5.4%
R_{ct} (Ω)	5.9	2.3	3.0
D_{Na^+} (cm^2 s^{-1})	4.12×10^{-12}	9.54×10^{-12}	5.17×10^{-12}
$R = L/\sigma A$ (Ω nm^{-1})	247–1237	17–28	1239–61 941
σ (S cm^{-1})	10–50	300–500	0.1–5
Specific capacitance (F g^{-1})	437	614	523

immigrate and distribute homogeneously, more V^{5+} ions become accessible at the surface region of samples for redox reactions, leading to an increased capacitance.[41] The wetting and electro-activation by the electrolyte might also increase the specific capacitance of electrodes during the cycling process.[42] The stability of Vö-V_2O_5/CP is superior to that of other SCs based on V_2O_5/PPy networks (81% capacitance retention after 1000 cycles),[21] V_2O_5/PPy (83% capacitance retention after 2000 cycles),[30] V_2O_5/PEDOT/MnO_2 (94% capacitance retention after 3000 cycles), and V_2O_5/PANI nanowires (92% capacitance retention after 5000 cycles).[33]

Conclusions

Oxygen vacancies (Vö) were generated in the near surface region of Vö-V_2O_5/CPs (CPs = PANI, PEDOT, and PPy) through the polymerization of CPs, and Vö induced a local electric field at the interface between the V_2O_5-NFs and CP coating. During charging and discharging processes, the local electric field promoted ion/electron transport, leading to enhanced charge transfer kinetics. The presence of V^{4+} and V^{3+} may catalyze the redox reactions and thus further enhance the electrochemical properties of Vö-V_2O_5/CPs. CP shells provided conductive charge transfer pathways to synergistically optimize the charge storage properties. As a result, Vö-V_2O_5/CP based supercapacitors delivered high specific capacitances of up to 614 F g^{-1} and excellent cycling stability over 15 000 cycles. It seems that both Vö and the nature of CPs have a significant impact on the electrochemical properties and device performance.

Conflicts of interest

There are no conflicts to declare.

Acknowledgements

This work is supported financially in part by the National Natural Science Foundation of China (grant no. U1503292 and 51872204), the Fundamental Research Funds for the Central Universities, and the National Key Research and Development Program of China (grant no. 2017YFA0204600). The work is also supported in part by the National Science Foundation (1803256). WCB was supported by the China Scholarship Council (CSC) for studying at the University of Washington. E. P. J. was supported by a subcontract from the National Institute of Standards and Technology. Opinions, recommendations, findings, and conclusions presented in this manuscript and associated materials do not necessarily reflect the views or policies of the NIST or the United States government.

Notes and references

1 T. Qin, B. Liu, Y. Wen, Z. Wang, X. Jiang, Z. Wan, S. Peng, G. Cao and D. He, *J. Mater. Chem. A*, 2016, **4**, 9196–9203.
2 L. Q. Mai, A. Minhas-Khan, X. Tian, K. M. Hercule, Y. L. Zhao, X. Lin and X. Xu, *Nat. Commun.*, 2013, **4**, 2923–2930.
3 G. Zhu, L. Yang, W. Wang, M. Ma, J. Zhang, H. Wen, D. Zheng and Y. Yao, *Chem. Commun.*, 2018, **54**, 9234–9237.
4 T. Yang, J. Liang, I. Sultana, M. M. Rahman, M. J. Monteiro, Y. Chen, Z. Shao, S. R. P. Silva and J. Liu, *J. Mater. Chem. A*, 2018, **6**, 8280–8288.
5 Q. Liu, H. Shi, T. Yang, Y. Yang, Z.-S. Wu, J. Yu, S. R. P. Silva and J. Liu, *J. Mater. Chem. A*, 2019, **7**, 6197–6204.
6 P. Ratajczak, M. E. Suss, F. Kaasik and F. Béguin, *Energy Storage Mater.*, 2018, **16**, 126–145.
7 P. Lu, X. Wang, L. Wen, X. Jiang, W. Guo, L. Wang, X. Yan, F. Hou, J. Liang, H. M. Cheng and S. X. Dou, *Small*, 2019, **15**, 1805064.
8 T. Yang, R. Zhou, D. W. Wang, S. P. Jiang, Y. Yamauchi, S. Z. Qiao, M. J. Monteiro and J. Liu, *Chem. Commun.*, 2015, **51**, 2518–2521.
9 F. Wang, X. Wu, X. Yuan, Z. Liu, Y. Zhang, L. Fu, Y. Zhu, Q. Zhou, Y. Wu and W. Huang, *Chem. Soc. Rev.*, 2017, **46**, 6816–6854.
10 Y. Wang, X. Fu, M. Zheng, W. H. Zhong and G. Cao, *Adv. Mater.*, 2019, **31**, 1804204–1804233.
11 G. Zhu, H. Wen, M. Ma, W. Wang, L. Yang, L. Wang, X. Shi, X. Cheng, X. Sun and Y. Yao, *Chem. Commun.*, 2018, **54**, 10499–10502.
12 Y. Zeng, Y. Han, Y. Zhao, Y. Zeng, M. Yu, Y. Liu, H. Tang, Y. Tong and X. Lu, *Adv. Energy Mater.*, 2015, **5**, 1402176.
13 X. Cao, B. Zheng, W. Shi, J. Yang, Z. Fan, Z. Luo, X. Rui, B. Chen, Q. Yan and H. Zhang, *Adv. Mater.*, 2015, **27**, 4695–4701.
14 Y. Wang and G. Z. Cao, *Chem. Mater.*, 2006, **18**, 2787–2804.
15 M. Ghosh, V. Vijayakumar, R. Soni and S. Kurungot, *Nanoscale*, 2018, **10**, 8741–8751.
16 T. Zhai, S. Xie, M. Yu, P. Fang, C. Liang, X. Lu and Y. Tong, *Nano Energy*, 2014, **8**, 255–263.
17 H. S. Kim, J. B. Cook, H. Lin, J. S. Ko, S. H. Tolbert, V. Ozolins and B. Dunn, *Nat. Mater.*, 2017, **16**, 454–460.
18 S. Yang, Y. Liu, Y. Hao, X. Yang, W. A. Goddard 3rd, X. L. Zhang and B. Cao, *Adv. Sci.*, 2018, **5**, 1700659–1700669.
19 Y. Lv, Z. Chen, Y. Liu, T. Wang and Z. Ming, *Nano-Struct. Nano-Objects*, 2018, **15**, 114–118.
20 C. X. Guo, G. Yilmaz, S. Chen, S. Chen and X. Lu, *Nano Energy*, 2015, **12**, 76–87.
21 T. Qian, N. Xu, J. Q. Zhou, T. Z. Yang, X. J. Liu, X. W. Shen, J. Q. Liang and C. L. Yan, *J. Mater. Chem. A*, 2015, **3**, 488–493.
22 F. Huguenin, M. Ferreira, V. Zucolotto, F. C. Nart, R. M. Torresi and O. N. Oliveira, *Chem. Mater.*, 2004, **16**, 2293–2299.
23 W. Bi, Y. Wu, C. Liu, J. Wang, Y. Du, G. Gao, G. Wu and G. Cao, *ACS Appl. Energy Mater.*, 2018, **2**, 668–677.
24 W. Bi, E. P. Jahrman, G. T. Seidler, J. Wang, G. Gao, G. Wu, M. Atif, M. S. AlSalhi and G. Cao, *ACS Appl. Mater. Interfaces*, 2019, **11**, 16647–16655.
25 G. T. Seidler, D. R. Mortensen, A. J. Remesnik, J. I. Pacold, N. A. Ball, N. Barry, M. Styczinski and O. R. Hoidn, *Rev. Sci. Instrum.*, 2014, **85**, 113906.
26 E. P. Jahrman, W. M. Holden, A. S. Ditter, D. R. Mortensen, G. T. Seidler, T. T. Fister, S. A. Kozimor, L. F. J. Piper, J. Rana,

N. C. Hyatt and M. C. Stennett, *Rev. Sci. Instrum.*, 2019, **90**, 024106–024121.
27 W. Bi, G. Gao, Y. Wu, H. Yang, J. Wang, Y. Zhang, X. Liang, Y. Liu and G. Wu, *RSC Adv.*, 2017, 7, 7179–7187.
28 A. T. Lawal and G. G. Wallace, *Talanta*, 2014, **119**, 133–143.
29 X. W. Zhou, G. M. Wu, J. D. Wu, H. Yang, J. Wang, G. Gao, R. Cai and Q. Yan, *J. Mater. Chem. A*, 2013, **1**, 15459–15468.
30 J. G. Wang, H. Liu, H. Liu, W. Hua and M. Shao, *ACS Appl. Mater. Interfaces*, 2018, **10**, 18816–18823.
31 C. Jiang, G. Chen and X. Wang, *Synth. Met.*, 2012, **162**, 1968–1971.
32 I. Šeděnková, M. Trchová and J. Stejskal, *Polym. Degrad. Stab.*, 2008, **93**, 2147–2157.
33 M. H. Bai, T. Y. Liu, F. Luan, Y. Li and X.-X. Liu, *J. Mater. Chem. A*, 2014, **2**, 10882–10888.
34 H. Wang, L. Bian, P. Zhou, J. Tang and W. Tang, *J. Mater. Chem. A*, 2013, **1**, 578–584.
35 P. Simon and Y. Gogotsi, *Nat. Mater.*, 2008, 7, 845–854.
36 D. O. Scanlon, A. Walsh, B. J. Morgan and G. W. Watson, *J. Phys. Chem. C*, 2008, **112**, 9903–9911.
37 Y. Zheng, T. Zhou, X. Zhao, W. K. Pang, H. Gao, S. Li, Z. Zhou, H. Liu and Z. Guo, *Adv. Mater.*, 2017, **29**, 1700396.
38 X. Zhao, H.-E. Wang, X. Chen, J. Cao, Y. Zhao, Z. Garbe Neale, W. Cai, J. Sui and G. Cao, *Energy Storage Mater.*, 2018, **11**, 161–169.
39 H. Song, C. Liu, C. Zhang and G. Cao, *Nano Energy*, 2016, **22**, 1–10.
40 G. A. Snook, P. Kao and A. S. Best, *J. Power Sources*, 2011, **196**, 1–12.
41 Y. Li, Y. Lei, B. G. Shen and J. R. Sun, *Sci. Rep.*, 2015, **5**, 14576.
42 Y. Yan, Q. Cheng, Z. Zhu, V. Pavlinek, P. Saha and C. Li, *J. Power Sources*, 2013, **240**, 544–550.